Single and double branched organic dyes based on carbazole and red-absorbing cationic indolium for p-type dye-sensitized solar cells: A combined experimental and theoretical investigation

Le Quoc Bao [a, b], Phuong Ho [a], Ramesh Kumar Chitumalla [c], Joonkyung Jang [c], Suresh Thogiti [a, *], Jae Hong Kim [a, **]

[a] School of Chemical Engineering, Yeungnam University, 214-1, Dae-dong, Gyeongsan, Gyeongbuk, 712-749, Republic of Korea
[b] Faculty of Applied Sciences, Ton Duc Thang University, 19 Nguyen Huu Tho Str., Tan Phong Ward, District 7, Ho Chi Minh City 700000, Viet Nam
[c] Department of Nanoenergy Engineering, Pusan National University, Busan, 609-735, Republic of Korea

ARTICLE INFO

ABSTRACT

A series of novel single and double branched carbazole-based red-absorbing cationic dyes without (CSI and CDI) and with (CST and CDT) a thiophene spacer have been synthesized for p-type dye-sensitized solar cells (p-DSSCs). The introduction of the red-absorbing cationic acceptor/thiophene spacer led to the broadening and bathochromic shift of the absorption maxima from an onset of 600 nm for CSI to 800 nm for CDT as well as improved molar absorptivity. The introduction of the double branching/ thiophene spacer lowered the lowest unoccupied molecular orbital (LUMO) levels of CDI, CST, and CDT, making their potentials more positive than that of CSI. Among these, the double branched CDI exhibited the highest conversion efficiency of 0.112%. Furthermore, all of the dyes examined outperformed the standard C343 dye (0.062%), measured under similar fabrication conditions. Despite the decreased photovoltaic performance as a result of the introduction of the thiophene spacer, overall, the double branched dyes exhibited better interfacial charge transfer that led to higher J_{SC} and V_{OC} values compared to those of singly branched dyes. Electrochemical impedance spectroscopy analysis showed that double branched dyes have much lower charge transfer resistance and increased hole lifetime than single branched dyes. Density functional theory (DFT) and time-dependent DFT calculations were performed to theoretically characterize the optical and electrochemical properties of the synthesized dyes.

1. Introduction

Dye-sensitized solar cells (DSSCs), developed by Grätzel et al. in the 1990s, are an attractive source of renewable energy and are typically perceived as a low-cost alternative to conventional silicon-based solar cells [1–3]. Two types of DSSCs exist, namely, DSSCs that employ n-type semiconductors such as TiO$_2$ as the photo-anode (n-DSSCs) [4], and their inverse model, p-DSSCs, which employ p-type semiconductors such as NiO [5]. Various solar cells have been prepared using n-type sensitizers, attaining enhanced power conversion efficiencies (PCEs) [4,6–12]. The dye sensitizers typically utilized in these n-DSSCs can absorb only in the visible or near-infrared (NIR) region of the solar spectrum. Currently, it is still challenging to synthesize dyes that are capable of covering both the visible and NIR regions. On the other hand, p-type devices have rarely been studied and their PCEs are generally significantly lower than those of n-type DSSCs [5,13–23]. The investigation of p-type DSSCs is motivated by the desire to combine them with traditional n-type DSSCs into tandem pn-DSSCs (TDSSCs), which can provide higher photo-voltage and potentially also a high PCE. Until now, however, the efficiencies of TDSSCs have been hampered by the poor performance of p-type DSSCs [24–28].

The operational principles of p-type DSSCs are illustrated in Fig. 1. In contrast to the n-type DSSC, the hole in the p-type DSSC is injected into the semiconductor and an electron is transferred to the electrolyte through a photo-excited sensitizer [5,29]. Among all of the components present, the sensitizer plays a key role in

* Corresponding author. Department of Chemical Engineering, Yeungnam University, Republic of Korea.
** Corresponding author. Department of Chemical Engineering, Yeungnam University, Republic of Korea.
E-mail addresses: sureshyu@ynu.ac.kr (S. Thogiti), jaehkim@yumail.ac.kr (J.H. Kim).
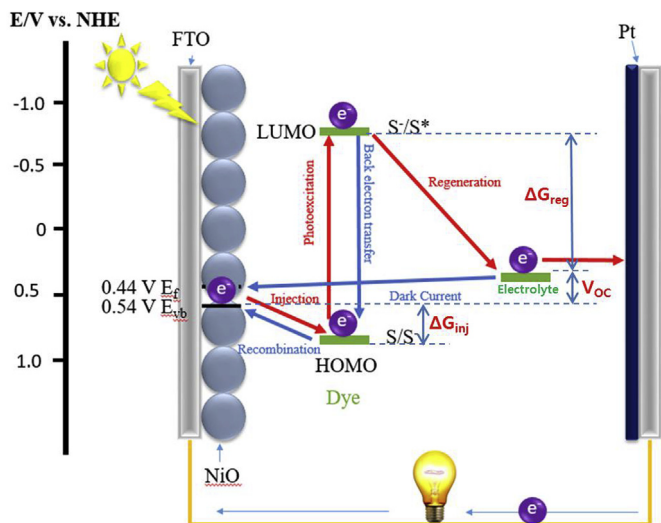
Fig. 1. Schematic representation of the construction and operational principles of a typical *p*-NiO-based dye-sensitized solar cell (DSSC). The generation of photocurrents is represented by red arrows, whereas the recombination processes are represented by blue arrows. (For interpretation of the references to colour in this figure legend, the reader is referred to the web version of this article.)

capturing photons, generating electron and hole pairs, and subsequently transferring them. For this reason, the design and development of new dye materials is in high demand. Owing to the fact that the efficiency of DSSCs depends significantly on the optimization and compatibility of each of its constituents, the sensitizers are expected to capture as many photons from the sunlight as possible. With the objective of developing new sensitizers for p-type DSSCs, we synthesized in this study four sensitizers (CSI-CDT) based on a well-known aromatic heterocycle, namely carbazole, which has been shown to provide potentially increased efficiencies in n-DSSCs [30—35]. The red-absorbing cationic 1-octyl-2,3,3-trimethyl-3H-indolium iodide was used as the acceptor in order to facilitate the fabrication of p-type DSSCs with improved performance, owing to the recent reports that showed that this compound can enable dyes to absorb long-wavelength visible light [36—39]. Earlier efforts to shift the absorption towards longer wavelengths by increasing the number of cyano moieties have led to diminished photocurrents in *p*-DSSCs. This outcome was attributed to the decrease in the driving force for dye regeneration, which resulted from the decrease in the level of the lowest unoccupied molecular orbital (LUMO). By introducing an indolium cationic acceptor, Wood et al. succeeded in maintaining sufficient driving force for dye regeneration while increasing the absorption in the red region [36].

Organic dyes with donor—acceptor-based double anchoring/ acceptor were reported to display improved efficiencies in n- and p-type DSSCs [37,40—45]. In 2014, Park et al. synthesized a donor—acceptor carbazole-based MCBZ (herein referred to as CSI) and DCBZ dye sensitizers for *p*-DSSCs, and obtained enhanced conversion efficiency of 0.035% for the double branched di-anchoring dye DCBZ. Taking into consideration the above described points, the single (CSI and CST) and double branched (CDI and CDT) carbazole-based photosensitizers are applied to p-type DSSCs and compared with standard C343 dye under similar fabrication conditions. The experimental results of UV-vis spectroscopy, cyclic voltammetry (CV), and electrochemical impedance spectroscopy (EIS), together with the incident photo-to-current conversion efficiencies (IPCEs), and the outcome of theoretical density functional theory (DFT) and time-dependent DFT (TDDFT)

calculations were examined to explain their structure—property relationships.

2. Experimental

2.1. Materials

All ^{1}H NMR spectra were recorded on a Varian Mercury NMR 300 MHz spectrometer using $CDCl_3$ or DMSO-d_6 as the solvent (purchased from Alfa Aesar). The ^{1}H NMR chemical shifts were referenced relative to TMS. The absorption spectra were recorded on an Agilent 8453 UV-vis spectrophotometer. The active areas of the dye-absorbed NiO films were estimated using a digital microscope camera equipped with an image-analysis-software (Moticam 1000). The photovoltaic I-V characteristics of the prepared DSSCs were measured under 1 sunlight intensity (100 mW/cm^2, AM 1.5), which was verified with an AIST-calibrated Si-solar cell (PEC-L11, Peccell Technologies, Inc., City, State, Country). The incident monochromatic photon-to-current efficiencies (IPCEs) were plotted as a function of the light wavelength using an IPCE measurement instrument (PEC-S20, Peccell Technologies, Inc.). The redox properties of three dyes were examined using cyclic voltammetry (Model: CV-BAS-Epsilon). The electrolyte solution employed in this analysis was 0.10 M tetrabutylammonium hexafluorophosphate (TBABF$_6$) in freshly dried acetonitrile. The Ag/AgCl and Pt wire (0.5 mm in diameter) electrodes were used as the reference and counter electrodes, respectively. The scan rate was set at 30 mV/s. Electrochemical impedance spectroscopy (EIS) was performed using an electronic-chemical analyzer (Iviumstat Tec.).

2.2. Preparation of sensitizers

Some of the starting compounds, *i.e.*, 1-bromohexane, 1-iodooctane, pyridine, and methanol were obtained from Sigma-Aldrich, whereas others such as carbazole, *N,N*-dimethylformamide (DMF), 4-hydrazinobenzoic acid, 3-methyl-2-butanone, 2-(tri-*n*-butylstannyl)thiophene, *trans*-dichlorobis(triphenyl-phosphine)palladium(II) (PdCl$_2$(PPh$_3$)$_2$) were purchased from Alfa Aesar. Phosphorus oxychloride (POCl$_3$) was obtained from DeaJung Co., Ltd., and all other solvents and components were purchased from Duksan Pure Chemicals Co., Ltd.

2.2.1. 5-Carboxyl-2,3,3-trimethyl-3H-indoline *(1)*

A mixture of 4-hyrazinobenzoic acid (10 g, 65.72 mmol), 3-methyl-2-butanone (8.49 g, 98.58 mmol) and sodium acetate (10.78 g, 131.449 mmol) in acetic acid were refluxed under nitrogen at 120 °C for 12 h. The resulting brown suspension was cooled to room temperature, the solvent was removed under reduced pressure, and a mixture of MeOH:H$_2$O (1:9) was added to the residue. The flask was cooled on ice to induce precipitation. The obtained residue was filtered and washed several times with hexane and diethyl ether to give **1** as a white powder (8.62 g, 64.57%). ^{1}H NMR (DMSO-d_6, 300 MHz) δ 12.79 (s, 1H), 7.99 (s, 1H), 7.93 (d, J = 7.8 Hz, 1H), 7.52 (d, J = 7.8 Hz, 1H), 2.25 (s, 3H), 1.28 (s, 6H).

2.2.2. 5-Carboxyl-2,3,3-trimethyl-1-octyl-3H-indoline, iodide (1:1) *(2)*

5-carboxyl-2,3,3-trimethyl-3H-indoline **1** (5.5 g, 36.14 mmol) was dissolved in acetonitrile (100 mL) and refluxed at 80 °C under nitrogen atmosphere and 1-iodooctane (21.12 g, 87.95 mmol) was added to this solution. After 72 h, the flask was cooled to room temperature and the solvent was removed under reduced pressure. The crude product was recrystallized from a mixture of acetonitrile and diethyl ether. The precipitate was filtered and washed several times with ether, hexane, and ethyl acetate to give **2** as a white solid

(4.68 g, 40%). ^{1}H NMR (DMSO-d$_6$, 300 MHz) δ 8.40 (s, 1H), 8.17 (d, $J = 7.8$ Hz, 2H), 4.48 (s, 2H), 2.89 (s, 3H), 1.84 (s, 2H), 1.58 (s, 6H), 1.33 (m, 10H), 0.85 (s, 3H).

2.2.3. 9-Hexylcarbazole (3)

Carbazole (15 g, 89.70 mmol) was dissolved in DMF (100 mL) and 1-bromohexane (23.90 g, 144 mmol) was added directly to the solution. The mixture was stirred under nitrogen at 80 °C for 6 h. After cooling to room temperature, the solvent was removed under reduced pressure. Next, MeOH was added to the solution and the mixture was kept on ice to yield the product **3** as a white crystalline precipitate (16.24 g, 72.75%). ^{1}H NMR (Acetone-d$_6$, 300 MHz) δ 8.17 (d, $J = 7.8$ Hz, 2H), 7.60 (d, $J = 8.1$ Hz, 2H), 7.50 (t, $J = 8.1$ Hz, 2H), 7.24 (t, $J = 7.8$ Hz, 2H) 4.47 (t, $J = 7.2$ Hz, 2H), 1.94 (p, $J = 7.5$ Hz, 2H), 1.45 (m, 6H), 0.89 (t, $J = 6.9$ Hz, 3H).

2.2.4. 9-Hexylcarbazole-3-carboxaldehyde (4)

9-hexylcarbazole **3** (6 g, 23.88 mmol) was dissolved in 1,2-dichloroethane (50 mL, DCE) in a three-necked round-bottom flask and the mixture was cooled on an ice bath. A mixture of DMF (2.8 g, 38.3 mmol) and POCl$_3$ (8 g, 52.17 mmol) in EtOH was added to the solution. The reaction was stirred at 80 °C under nitrogen. After 6 h, the reaction was cooled to room temperature and an aqueous solution of NaOH was added slowly to quench the reaction. The organic fraction was extracted with chloroform, dried over anhydrous CaCl$_2$, filtered, and the solvent was removed under reduced pressure. The residue was purified by silica gel column chromatography using hexane:DCM (1:1) as the eluent. The desired product **4** was obtained as a white solid (5.3 g, 80.34%). ^{1}H NMR (CDCl$_3$, 300 MHz) δ 10.09 (s, 1H), 8.61 (s, 1H), 8.17 (d, $J = 7.8$ Hz, 1H), 8.02 (d, $J = 8.4$ Hz, 1H), 7.56 (m, 3H), 7.35 (t, $J = 7.5$ Hz, 1H), 4.35 (t, $J = 7.2$ Hz, 2H), 1.91 (t, $J = 7.2$ Hz, 2H), 1.39 (m, 6H), 0.88 (t, $J = 6.9$ Hz, 3H).

2.2.5. 9-Hexylcarbazole-3-[2-(5-carboxyl-2,3,3-trimethyl-1-octyl-3H-indoline)ethenyl], iodide (CSI)

A mixture of 9-hexylcarbazole-3-carboxaldehyde **4** (0.5 g, 1.79 mmol) and 5-carboxyl-2,3,3-trimethyl-1-octyl-3H-indoline **1** (1.26 g, 1.6 equiv.) was dissolved in MeOH, and refluxed under nitrogen for 7 h at 70 °C. After this time, the solution was cooled to room temperature and the solvent was removed under reduced pressure. The residue was recrystallized from diethyl ether, and the precipitate was washed several times with ethyl acetate to give **CSI** as a red solid (0.92 g, 72.93%). ^{1}H NMR (DMSO-d$_6$, 300 MHz) δ 13.36 (s, 1H), 9.13 (s, 1H), 8.82 (d, $J = 15.6$ Hz, 1H), 8.43 (d, $J = 6.6$ Hz, 2H), 8.25 (d, $J = 7.2$ Hz, 1H), 8.19 (d, $J = 8.4$ Hz, 1H), 7.99 (d, $J = 9$ Hz, 1H), 7.87 (d, $J = 8.7$ Hz, 1H), 7.77—7.69 (t, 2H), 7.61 (t, $J = 7.5$ Hz, 1H), 7.41 (t, $J = 7.5$ Hz, 1H), 4.75 (t, $J = 6.9$ Hz, 2H), 4.54 (t, $J = 6.9$ Hz, 2H), 1.90 (m, 10H), 1.45 (m, 16H), 0.82 (q, 6H).

2.2.6. 9-Hexylcarbazole-3,6-dicarboxaldehyde (5)

9-hexylcarbazole-3-carboxaldehyde **4** (2 g, 7.96 mmol) was dissolved in DCE (50 mL) and kept at 0 °C while DMF (16 g, 2.18 mmol) and POCl$_3$ (20 g, 13.04 mmol) were added slowly. After 2 h of stirring under nitrogen, the solution was heated to 90 °C and maintained at this temperature for 7 h. The reaction was cooled to room temperature and quenched by the slow addition of NaOH (200 mL, 2 M) solution. The organic fractions were extracted with chloroform, dried over anhydrous CaCl$_2$, and filtered. Subsequently, the solvent was removed under reduced pressure and the crude residue was purified by silica gel column chromatography using a mixture of hexane:DCM (1:1) as the eluent. The final product **5** was obtained as a white solid (0.67 g, 27.27%). ^{1}H NMR (CDCl$_3$, 300 MHz) δ 10.14 (s, 2H), 8.68 (s, 2H), 8.11 (d, $J = 8.1$ Hz, 2H), 4.41 (t, $J = 7.2$ Hz, 2H), 1.94 (m, $J = 7.5$ Hz, 2H), 1.43 (m, 6H), 0.89 (t, $J = 7.2$ Hz, 3H).

2.2.7. 9H- carbazole, 9-hexyl-3,6-bis-[2-(5-carboxyl-2,3,3-trimethyl-1-octyl-3H-indoline)ethenyl]-, iodide (CDI)

9-hexylcarbazole-3,6-dicarboxaldehyde **5** (0.5 g, 1.62 mmol) and 5-carboxyl-2,3,3-trimethyl-1-octyl-3H-indoline, iodide (1:1) **2** (2 g, 4.51 mmol) were dissolved in MeOH. The subsequent reaction steps were identical to those described for the synthesis of **CSI**. The target **CDI** was obtained as a dark red solid (0.93 g, 49.36%). ^{1}H NMR (DMSO-d$_6$, 300 MHz) δ 13.37 (s, 2H), 9.24 (s, 2H), 8.82 (d, $J = 15.6$ Hz, 2H), 8.54 (d, $J = 7.8$ Hz, 2H), 8.45 (s, 2H), 8.21 (d, $J = 8.4$ Hz, 2H), 8.04 (t, $J = 8.4$ Hz, 4H), 7.85 (d, $J = 15.6$ Hz, 2H), 4.80 (t, $J = 6.9$ Hz, 4H), 4.63 (t, $J = 6.9$ Hz, 2H), 1.92 (m, 18H), 1.47—1.21 (m, 26H), 0.82 (q, 9H).

2.2.8. 3-Bromo-9-hexylcarbazole (6)

NBS (2.76 g, 15.52 mmol) was dissolved in a mixture of DCE (80 mL) and THF (20 mL) and added drop-wise to the solution 9-hexylcarbazole **3** (3 g, 11.94 mmol) dissolved in DCE (50 mL) in a three-necked round-bottom flask and stirred under nitrogen from 0 °C to ambient temperature. After 6 h, the solution was extracted with DCM, dried over anhydrous CaCl$_2$, and filtered. The solvent was removed under reduced pressure to yield the crude product, which was purified by silica gel column chromatography with 90% hexane:DCM as the eluent to give **6** as a white solid (3.2 g, 81.41%). ^{1}H NMR (Acetone-d$_6$, 300 MHz) δ 8.41—8.19 (q, 2H), 7.62—7.49 (m, 4H), 7.28 (t, $J = 7.5$ Hz, 1H), 4.48 (t, $J = 7.2$ Hz, 2H), 1.91 (m, $J = 6.6$ Hz, 2H), 1.31 (m, 6H), 0.88 (t, $J = 6.6$ Hz, 3H).

2.2.9. 9-Hexylcarbazole-3-(2-thienyl) (7)

3-bromo-9-hexylcarbazole **6** (2.6 g, 7.9 mmol), 2-(tri-n-butyl-stannyl)thiophene (4.7 g, 12.6 mmol) and PdCl$_2$(PPh$_3$)$_2$ (0.55 g, 0.79 mmol) were dissolved in pyridine (30 mL) and refluxed at 90 °C under nitrogen. After 18 h, the mixture was cooled to room temperature, the organic components were extracted with ethyl acetate, dried over anhydrous Na$_2$SO$_4$, and filtered. The residue obtained after the solvent was evaporated under reduced pressure was purified by silica gel column chromatography with 5—10% ethyl acetate in hexane as the eluent. The final product **7** was acquired as a yellow solid (0.83 g, 31.53%). ^{1}H NMR (CDCl$_3$, 300 MHz) δ 8.34 (d, $J = 9$ Hz, 1H), 8.14 (d, $J = 7.2$ Hz, 1H), 7.74 (d, $J = 8.4$ Hz, 1H), 7.50 (t, $J = 7.8$ Hz, 1H), 7.41—7.33 (m, 3H), 7.24 (d, $J = 7.5$ Hz, 2H), 7.12 (t, $J = 3.6$ Hz, 1H), 4.32 (t, $J = 7.2$ Hz, 2H), 1.92 (m, $J = 7.2$ Hz, 2H), 1.42 (m, 6H), 0.89 (t, $J = 7.2$ Hz, 3H).

2.2.10. 5-(9-hexyl-9H-carbazole-3-yl)thiophene-2-carbaldehyde (8)

9-hexylcarbazole-3-(2-thienyl) **7** (0.5 g, 1.5 mmol) was dissolved in DCE (20 mL) and stirred in a three-necked round-bottom flask from 0 °C to ambient temperature under nitrogen atmosphere. A mixture of DMF (0.15 g, 2.1 mmol) and POCl$_3$ (0.46 g, 3 mmol) in DCE (20 mL) was added slowly to this solution and the mixture was maintained for 1 h before being heated to 70 °C. After 2 h, the solution was cooled to room temperature and an aqueous solution of NaOH (2 M) was added slowly to quench the reaction. The mixture was extracted with DCM, dried over anhydrous CaCl$_2$, filtered, and the solvent removed under reduced pressure. The crude product was purified by silica gel column chromatography using 10% ethyl acetate in hexane as the eluent to give **8** as a yellow solid (0.36 g, 66.41%). ^{1}H NMR (Acetone-d$_6$, 300 MHz) δ 9.93 (s, 1H), 8.63 (s, 1H), 8.29 (d, $J = 7.2$ Hz, 1H), 7.97—7.89 (q, 2H), 7.70—7.61 (m, 3H), 7.54 (t, $J = 7.2$ Hz, 1H), 4.50 (t, $J = 7.2$ Hz, 2H), 1.93 (m, $J = 7.5$ Hz, 2H), 1.42 (m, 6H), 0.87 (t, $J = 6.9$ Hz, 3H).

2.2.11. 5-(9-hexyl-9H-carbazole-3-yl)thiophene-2-[5-carboxyl-2,3,3-trimethyl-1-octyl-3H-indoline], iodide (CST)

5-(9-hexyl-9H-carbazole-3-yl)thiophene-2-carbaldehyde **8**

(0.3 g, 0.83 mmol) was dissolved in DCE (30 mL) and mixed with 5-carboxyl-2,3,3-trimethyl-1-octyl-3H-indoline, iodide (1:1) **2** (0.55 g, 1.24 mmol) dissolved in MeOH (70 mL) in a three-necked round-bottom flask. The mixture was refluxed at 70 °C for 12 h under nitrogen atmosphere. After this time, the mixture was cooled to room temperature. The subsequent work-up and purification steps were identical to those described for the preparation of **CSI**. The final product **CST** was obtained as a dark blue solid (0.3 g, 45.93%). ^{1}H NMR (DMSO-d_6, 300 MHz) δ 8.85−8.73 (t, 2H), 8.40 (s, 1H), 8.32 (d, $J = 3.9$ Hz, 1H), 8.27 (d, $J = 7.5$ Hz, 1H), 8.17 (d, $J = 8.4$ Hz, 1H), 7.98−7.93 (m, 3H), 7.78 (d, $J = 8.7$ Hz, 1H), 7.69 (d, $J = 8.4$ Hz, 1H), 7.56 (t, $J = 7.2$ Hz, 1H), 7.32−7.20 (m, 2H), 4.64 (t, $J = 7.2$ Hz, 2H), 4.48 (t, $J = 7.2$ Hz, 2H), 1.85 (m, 10H), 1.44−1.21 (m, 17H), 0.83 (t, $J = 6.9$ Hz, 6H).

2.2.12. 3,6-Dibromo-9-hexylcarbazole (**9**)

NBS (8.5 g, 47.76 mmol) was dissolved in a mixture of DCE (80 mL) and THF (20 mL) and added to a solution 9-hexylcarbazole **3** (3 g, 11.94 mmol) in DCE (50 mL). The mixture was stirred under nitrogen, while the temperature was allowed to increase from 0 °C to ambient temperature over 6 h. After this time, the mixture was extracted with DCM, and the organic layer was dried over CaCl$_2$ and filtered. The residue obtained after the solvent was removed under reduced pressure was purified using silica gel column chromatography with 50% DCM:hexane mixture as the eluent to give **9** as a white solid (4.2 g, 86.4%). ^{1}H NMR (CDCl$_3$, 300 MHz) δ 8.14 (s, 2H), 7.56 (d, $J = 7.2$ Hz, 2H), 7.28 (d, $J = 7.2$ Hz, 2H), 4.26 (t, $J = 7.2$ Hz, 2H), 1.87 (m, $J = 7.5$ Hz, 2H), 1.52 (m, 6H), 1.26 (t, $J = 7.5$ Hz, 3H).

2.2.13. 9-Hexylcarbazole-3,6-di-(2-thienyl) (**10**)

3,6-dibromo-9-hexylcarbazole **9** (2.5 g, 6.14 mmol), 2-(tri-*n*-butylstannyl)thiophene (7.35 g, 19.66 mmol), and PdCl$_2$(PPh$_3$)$_2$ (0.43 g, 0.61 mmol) were mixed in pyridine and refluxed at 90 °C under nitrogen. After 30 h, the mixture was cooled to room temperature and extracted with DCM. The organic layer was dried over CaCl$_2$ and the solvent was removed under reduced pressure. The crude residue was purified by silica gel column chromatography with 80% hexane:DCM as the eluent to give **10** as a yellow solid (1.07 g, 41.95%). ^{1}H NMR (CDCl$_3$, 300 MHz) δ 8.34 (s, 2H), 7.27 (d, 2H), 7.75 (d, $J = 7.2$ Hz, 2H), 7.40 (m, 4H), 7.13 (t, $J = 4.8$ Hz, 2H), 4.32 (t, $J = 7.2$ Hz, 2H), 1.93 (m, $J = 7.2$ Hz, 2H), 1.39 (m, 2H), 0.89 (t, $J = 6.9$ Hz, 3H).

2.2.14. 5,5'-(9-hexyl-9H-carbazole-3,6-diyl)thiophene-2-carbaldehyde (**11**)

9-hexylcarbazole-3,6-di-(2-thienyl) **10** (0.5 g, 1.2 mmol) was dissolved in DCE and stirred under nitrogen while the temperature was allowed to increase from 0 °C to ambient temperature. DMF (0.95 g, 13 mmol) and POCl$_3$ (3.2 9 g, 21.45 mmol) were dissolved in DCE and added slowly to the solution. After 1 h of stirring, the mixture was heated to 70 °C and refluxed for 8 h before being quenched by cooling to room temperature and slow addition of an aqueous solution of NaOH (2 M). The mixture was extracted with DCM, the organic layer was dried over anhydrous CaCl$_2$, and the solution filtered. The residue obtained after the solvent was removed under reduced pressure was purified using silica gel column chromatography with 70% hexane:DCM as the eluent. The target product **11** was obtained as a yellow solid (0.46 g, 81%). ^{1}H NMR (CDCl$_3$, 300 MHz) δ 9.90 (s, 2H), 8.44 (s, 2H), 7.84 (m, 4H), 7.49 (t, 4H), 4.36 (t, $J = 7.2$ Hz, 2H), 1.92 (p, $J = 6.9$ Hz, 2H), 1.40 (m, 6H), 0.89 (t, $J = 6.9$ Hz, 3H).

2.2.15. 5,5'-(9-hexyl-9H-carbazole-3,6-diyl)thiophene-2-[5-carboxyl-2,3,3-trimethyl-1-octyl-3H-indoline], iodide (CDT)

5,5'-(9-hexyl-9H-carbazole-3,6-diyl)thiophene-2-carbaldehyde

11 (0.3 g, 0.64 mmol) was dissolved in DCE (30 mL) in a three-necked round-bottom flask. To this solution, 5-carboxyl-2,3,3-trimethyl-1-octyl-3H-indoline, iodide (1:1) **2** (0.85 g, 1.9 mmol) dissolved in MeOH (50 mL) was added and the mixture was refluxed under nitrogen for 12 h at 70 °C. After this time, the mixture was cooled to room temperature. The subsequent purification steps were identical to those described for the synthesis of **CDI**. The final product **CDT** was obtained as a dark blue solid (0.53 g, 62.99%). ^{1}H NMR (DMSO-d_6, 300 MHz) δ 8.88 (t, 4H), 8.41 (s, 2H), 8.35 (d, $J = 3.9$ Hz, 2H), 8.18 (d, $J = 8.1$ Hz, 2H), 8.02 (t, 6H), 7.81 (d, $J = 8.7$ Hz, 2H), 7.28 (d, $J = 15.3$ Hz, 2H), 4.63 (b, 4H), 4.52 (b, 4H), 1.86 (b, 18H), 1.40 (m, 26H), 0.84 (t, $J = 6.3$ Hz, 9H).

2.3. Details of computational analysis

All calculations reported in this work were carried out using the Gaussian 09 suite of programs [46]. Ground state geometries of the four dyes were fully optimized without imposing any symmetry constraints by employing the B3LYP functional [47−49], which represents a combination of Becke's three-parameter hybrid treatment with the Lee−Yang−Parr correlation. To model the dyes, we replaced all of the long hexyl and octyl chains with simple methyl groups for computational simplicity and speed. As the alkyl chains have hardly any influence on the electrochemical and spectral properties of the dyes, we opted for small methyl groups. The effect of the solvent (acetonitrile) was taken into account using the integral equation formalism for the polarizable continuum model (PCM) [50,51] within the self-consistent reaction field theory. For all atoms, we used the standard 6-31G(d) polarized double-ξ quality basis set. Based on the optimized ground state geometries, we performed TDDFT simulations to obtain the excitation energies of the dyes in the UV-vis absorption region. The optical properties of the dyes were also calculated using a long-range corrected functional such as CAM-B3LYP.

2.4. Assembly and characterization of DSSCs

The NiO paste was prepared by mixing a slurry of NiO nanopowder (6 g) in ethanol with ethanolic ethyl cellulose solution (20 mL, 10 wt%), and terpinol (40 mL), and subsequently removing ethanol under reduced pressure. The conducting glass substrates (composed of fluorine-doped tin oxide, FTO) were cleaned successively with soapy water, ethanol, and acetone using an ultrasonic bath for 20 min. The mesoporous NiO layer was deposited using the doctor-blade technique on top of the bare FTO and compact NiO-blocking layer coated on top of the FTO. The films were dried at 70 °C for 45 min and sintered at 450 °C for 30 min. Subsequently, the resultant films with an active cell area of 0.24 cm^2 were immersed in 0.3 mM solution of sensitizers in dry acetonitrile for 48 h at 25 °C for dye absorption.

The counter electrodes were produced using a single drop of H$_2$PtCl$_6$ in isopropanol solution. This prepared mixer was applied to a clean FTO glass, which was subsequently thermally decomposed by annealing at 450 °C for 30 min. The complete device was assembled by placing a platinum-coated FTO substrate and a dyed NiO working electrode face-to-face using a 60 μm thick Surlyn (Dupont 1702). A solution of 1.4 M LiI and 0.1 M iodine in acetonitrile was used as the electrolyte, which was injected through a pre-drilled hole on the counter electrode.

3. Results and discussion

3.1. Synthesis

Generally, the multi-branching concept in organic dye-

sensitizers is expected to facilitate increased semiconductor surface, thus leading to a better photovoltaic performance. This effect has been observed for many organic dyes. In the majority of p-type dyes, the extension of π-conjugation can result in improved photovoltaic performance. In this work, the red-absorbing cationic indolium was selected as an acceptor owing to the recent reports that showed that the use of this compound can enable dyes to absorb long wavelength visible light, leading to improved performance of p-type DSSCs [36–39]. With these points in mind, we have designed and synthesized in the present work four novel carbazole-based single and double branched dye molecules with and without thiophene spacers. The synthetic routes to these four dyes are shown in Scheme 1, and are based on the procedure published by Park et al. [37] The 5-carboxy-2,3,3-trimethyl-1-octyl-3H-indolium iodide acceptor (**2**) was synthesized following the procedure published by Park et al. [37] Intermediate **3** was prepared from a simple carbazole via alkylation reaction with 1-bromohexane. In order to prepare the thiophene-conjugated dyes, intermediate **3** was subjected to mono and di-bromination, followed by Stille coupling to obtain intermediates **7** and **10**, respectively. In the next step, intermediates **3**, **7**, or **10** were

subjected to single or double Vilsmeier-Haack formylation to obtain intermediate **4** and **5** or **8** and **11**, respectively. In the final step, the target dye molecules, CSI, CDI, CST, and CDT, were obtained in reasonably good yields by Knoevenagel condensation reactions of aldehydes **4**, **5**, **8**, and **11** with 5-carboxy-2,3,3-trimethyl-1-octyl-3H-indolium iodide **2**, respectively.

3.2. Optical properties

UV-vis absorption spectra of the synthesized dye-sensitizers in acetonitrile are shown in Fig. 2a, and the corresponding data are listed in Table 1. Two major absorption bands were observed, namely a relatively weak band in the near-UV region (340–365 nm) corresponding to the π–π* electron transition, and a strong absorption in the visible region (440–600 nm) that could be assigned to an intramolecular charge transfer (ICT) between the donor unit and the acceptor end group. For the above four dyes, the double anchoring dyes CDI (541 nm and 63,101 M^{-1} cm^{-1}) and CDT (601 nm and 77,577 M^{-1} cm^{-1}) exhibited considerably more red-shifted and improved molar extinction coefficients (ε) than the congener of mono anchoring dyes CSI (520 nm and
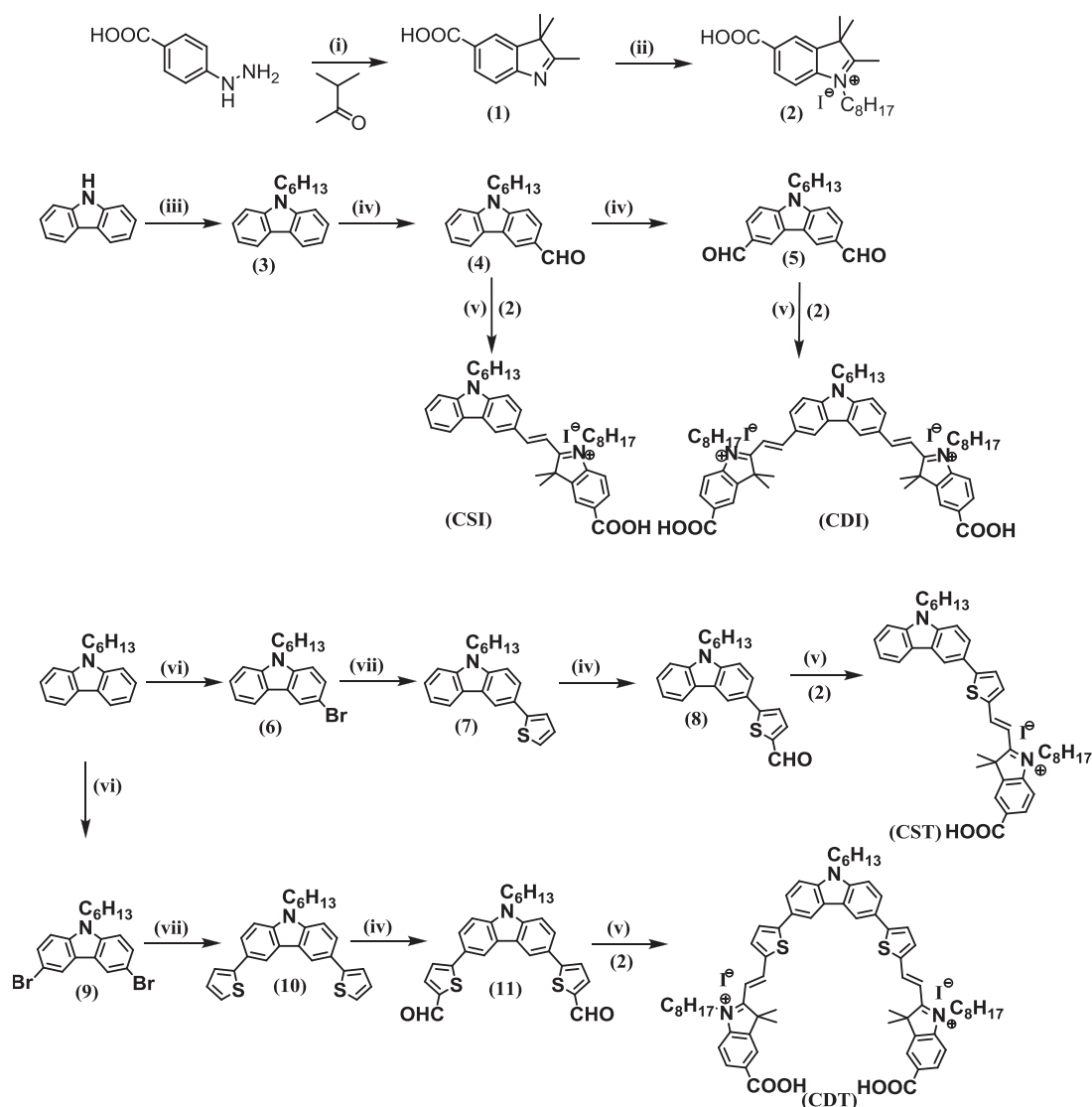
Scheme 1. Conditions and reagents employed in the syntheses of CSI, CDI, CST, and CDT dye sensitizers: (i) CH_3COONa, CH_3COOH, 120 °C, 12 h; (ii) 1-iodooctane, AcCN, 80 °C, 72 h; (iii) 1-bromohexane, NaH, DMF, 80 °C, 6 h; (iv) DMF, $POCl_3$, 90 °C, 7 h; (v) MeOH, 70 °C, 7 h; (vi) NBS, DCE, THF, 0 °C; (vii) 2-(tri-n-butylstannyl)thiophene, $PdCl_2(PPh_3)_2$, 90 °C, 18 h.
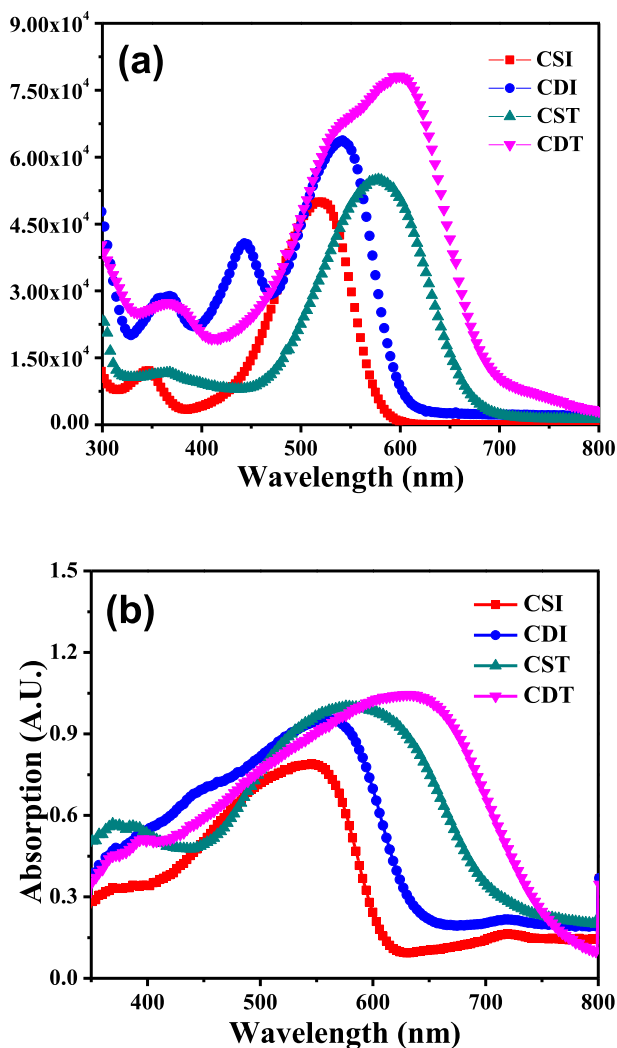
Fig. 2. The absorption spectra of (a) sensitizers in acetonitrile solution and (b) NiO films cast from acetonitrile solutions of CSI, CDI, CST, and CDT.

$50,171$ M^{-1} cm^{-1}) and CST (578 nm and $54,811$ M^{-1} cm^{-1}), respectively. In addition, irrespective of the anchoring number, the introduction of a thiophene spacer in CST and CDT resulted in a higher and broader absorption pattern. Overall, the double anchoring dyes CDI and CDT dyes displayed higher values of ε, while the mono anchoring dyes CSI and CST dyes showed lower values. The absorption peak wavelengths and the onset

wavelengths could be ordered from long to short as CDT > CST > CDI > CSI. Fig. 2b shows the absorption spectra of the four dyes on NiO films, where the NiO films were soaked in the dye solutions for 24 h. The relevant values are summarized in Table 1. The absorption maxima peaks for CSI, CDI, CST, and CDT on NiO films were at 545, 560, 580, and 632 nm, respectively. The absorption spectra of these dyes were broadened and red-shifted by 25, 19, 2, and 31 nm, respectively, when compared to their spectra in solution (Fig. 2a). These changes are indicative of strong interactions formed between the dyes and the semiconductor. Especially, CDT provided a panchromatic absorption wavelength.

3.3. Electrochemical properties

The ground-state oxidation and reduction potentials of the four prepared dyes were measured by CV in dry acetonitrile containing 0.1 M TBA(BF$_4$) at a 30 mV/s scan rate (Fig. 3). In each case, the highest occupied molecular orbital (HOMO) and the LUMO of the synthesized dye-sensitizers should provide adequately large driving force when compared to the NiO valence band and redox couple for successful charge transfer to occur. Table 1 shows the oxidation potentials (estimated HOMO levels) of the four sensitizers, which were found to be similar to each other (0.86–0.89 V) *vs.* NHE. These values are higher than the valence band potential of NiO (0.54 V) [38].

These higher values of HOMO levels could easily lead to the injection of electrons from the valence band of the NiO semiconductor into the sensitizers, or in other words, the hole could be distributed from the sensitizer to the NiO valence band (Fig. 4). The increase in conjugation as a result of the insertion of a heteroaromatic thiophene unit or changing from single branched to double branched resulted in red-shifted absorption pattern and subsequently, a decrease in the energy bandgap E_{0-0} [13,38]. The values of LUMO levels, which were extracted from the difference between E_{ox} and E_{0-0}, were found to be in the range from -0.91 to -1.37 V *vs.* NHE. These values are more negative than the redox potential of E (I_3^-/I_2^-) (-0.19 V *vs.* NHE). It is well known that the number of anchoring/electron accepting group has an influence on the LUMO level of dyes, and strong electron-accepting ability generally corresponds to lower lying LUMO. This will result in a lower thermodynamic driving force for dye regeneration. However, a strong electron-accepting group should increase the push-pull nature of the dye and improve the efficiency of charge separation within the molecule. The driving forces for hole injection (Eq. (1)) and dye regeneration (Eq. (2)) can be calculated according to the following equations [52]:

$$\Delta G_{inj} = e[E_{VB}(NiO) - (E_{0-0}(S^*) + E_{red}\ (S/S^-))] \tag{1}$$

Table 1
Optical and electrochemical data of sensitizers based on CSI, CDI, CST, and CDT.

Dye	ε x 10^4 ($M^{-1}cm^{-1}$)	λ_{max} (nm)		E_{0-0} (-V)[c] (abs)	E_{ox}[d] (V vs. NHE)	E_{ox}-E_{0-0}[e] (Vvs. NHE)	ΔG_{inj}[f] (-eV)	ΔG_{reg}[g] (-eV)
		Sol.[a]	Film[b]					
CSI	5.01	520	545	2.25	0.88	-1.37	-0.34	-1.18
CDI	6.31	541	560	2.07	0.89	-1.18	-0.35	-0.99
CST	5.48	578	580	1.84	0.87	-0.97	-0.33	-0.78
CDT	7.75	601	632	1.77	0.86	-0.91	-0.32	-0.72

[a] The absorption maxima of the dyes measured in acetonitrile.
[b] Absorption maxima of the dyes adsorbed onto the NiO films.
[c] The zero–zero transition energy (E0–0(S*)) was estimated from the onset absorption spectra.
[d] The ground-state oxidation potential (Eox) of the dyes were measured in dry acetonitrile.
[e] Eox−E0−0 = ELUMO.
[f] Calculated according to the equation: ΔGinj = e[EVB(NiO) − (E0−0(S*) + Ered (S/S−))], EVB(NiO) = 0.54 V vs NHE.
[g] Calculated according to the equation: ΔGreg = e[E(M/M−) − Ered(S/S−)], E(I3−/I2−·) = −0.19 V vs NHE.
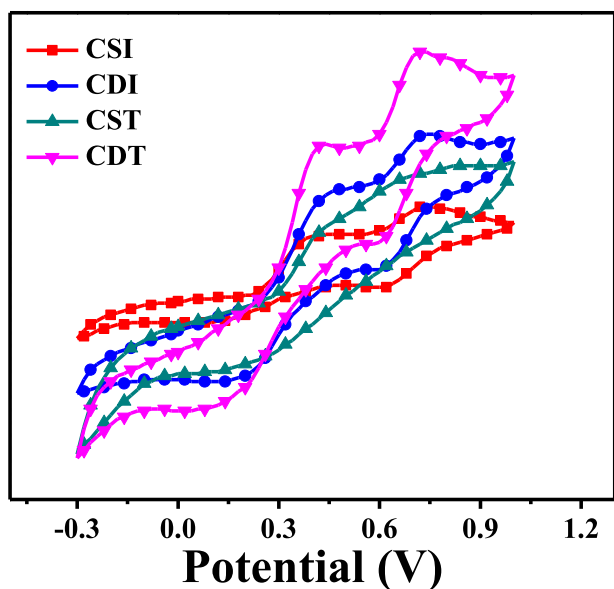
Fig. 3. Cyclic voltammograms of CSI, CDI, CST, and CDT in acetonitrile.

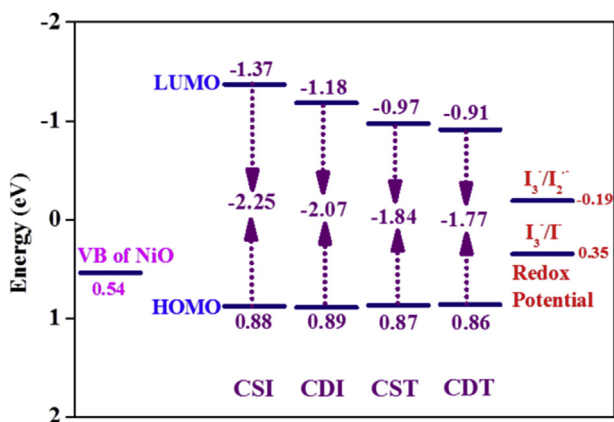**Fig. 4.** Energy level diagrams of CSI, CDI, CST, and CDT.

$$\Delta G_{reg} = e[E(M/M^-) - E_{red}(S/S^-)] \qquad (2)$$

These higher values of HOMO levels could easily lead to the injection of electrons from the valence band of the NiO semiconductor into the sensitizers, or in other words, the hole could be distributed from the sensitizer to the NiO valence band (Fig. 4). The increase in conjugation as a result of the insertion of a hetero-aromatic thiophene unit or changing from single branched to double branched resulted in red-shifted absorption pattern and subsequently, a decrease in the energy bandgap E_{0-0} [13,38]. The values of LUMO levels, which were extracted from the difference between E_{ox} and E_{0-0}, were found to be in the range from -0.91 to -1.37 V vs. NHE. These values are more negative than the redox potential of E (I_3^-/I_2^{--}) (-0.19 V vs. NHE). It is well known that the number of anchoring/electron accepting group has an influence on the LUMO level of dyes, and strong electron-accepting ability generally corresponds to lower lying LUMO. This will result in a lower thermodynamic driving force for dye regeneration. However, a strong electron-accepting group should increase the push-pull nature of the dye and improve the efficiency of charge separation within the molecule. The driving forces for hole injection (Eq. (1)) and dye regeneration (Eq. (2)) can be calculated according to the following equations [52]:

3.4. Theoretical calculations

DFT and TDDFT studies were performed on the four dyes to obtain a deeper understanding of their structural, electronic, electrochemical, and optical properties. The experimental optical and electrochemical properties of the dyes were corroborated by these theoretical results. While dyes CSI and CDI are planar in nature, the introduction of the thiophene ring in CST and CDT dyes disturbs this planarity. Fig. 5 shows the optimized ground state geometries of the four sensitizers, and Fig. 6 displays the electron density distributions in the frontier molecular orbitals of the modeled sensitizers. In the HOMO of all sensitizers, the electron density was predominantly localized over the carbazole moiety and partly delocalized over the rest of the molecule, with the exception of the anchoring group. By contrast, the electron densities of the LUMOs were shifted away from the carbazole moiety and spread onto the anchoring groups instead. Similar electron density distribution patterns have been observed previously for reported p-type organic sensitizers [53].

For effective hole injection in a p-type DSSC, the HOMO of the dye should be located well below the valence band edge of the semiconductor (-4.98 eV for NiO). The calculated HOMOs of the four dyes were below the valence band edge of NiO, which should ensure efficient hole injection in each case. Another requirement for p-type DSSC is that the LUMO of the dye should be well above the redox potential of the redox couple (-4.80 eV for I^-/I_3^-) for efficient dye regeneration process. It can be seen from Table 2 that the calculated LUMO levels of all sensitizers were above the redox potential of I^-/I_3^-, which facilitates effective dye regeneration. All simulated HOMO, LUMO eigenvalues, and HOMO–LUMO energy gaps are provided in Table 2, and are found to be in good agreement with those obtained experimentally using cyclic voltammetry. The HOMO–LUMO energy gaps decreased on going from CSI, to CDI, CST, and CDT, producing a bathochromic shift in the UV-vis absorption spectra of these dyes.

Simulated UV-vis absorption spectra. The UV-vis absorption spectra of the four sensitizers were simulated at the TD-B3LYP/6-31G(d) level of theory in acetonitrile. In these TDDFT simulations, 25 of the lowest singlet–singlet transitions were evaluated to obtain the optical properties of the four dyes. The simulated absorption spectra of the dyes are depicted in Fig. 7, and the calculated excitation wavelengths, oscillator strengths, and coefficients of configuration interaction are summarized in Table 3. The TDDFT simulations reproduced the main bands that were observed in the experimental UV-vis spectra of the four dyes. The spectrum of each dye exhibited two main bands, one below 500 nm and the second above 500 nm, with a tail extending to 800 nm. The calculated results revealed that the most intense transitions in the low-energy region were found at 499, 541, 615, and 660 nm for CSI, CDI, CST, and CDT, respectively. The theoretical results obtained for dyes CSI and CDI were in excellent agreement with the experimental absorption data. For dyes CST and CDT, however, the simulated absorption maxima varied somewhat from the experimental data, a fact that may be attributed to the inherent limitations of the TDDFT methodology to reproduce extended π systems [54].

The calculated absorption maxima of the dyes followed the same trend as observed experimentally. A considerable bathochromic shift in the absorption spectra was observed on going from CSI to CDT, which arises as a result of decreased HOMO-–LUMO energy gaps as the extent of π-conjugation increased. We also calculated the absorption spectra of the dyes using the range-separated functional CAM-B3LYP, but the results obtained using this method were not in a good agreement with the experimental
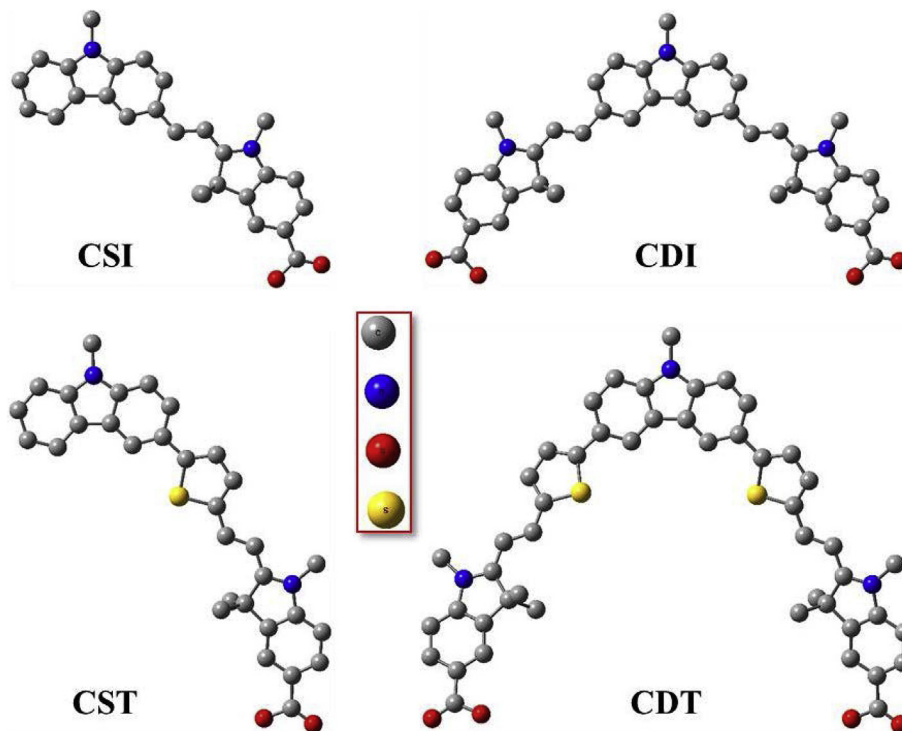
Fig. 5. Optimized ground state molecular geometries of CSI, CDI, CST, and CDT obtained at the B3LYP/6-31G(d) level of theory. Hydrogen atoms were omitted for clarity.

data. The optical properties of the dyes obtained using the CAM-B3LYP method are nonetheless provided in Table S1. The introduction of the thiophene ring produced a bathochromic shift on going from CSI to CST and from CDI to CDT. Because of the improvements in optical properties observed as a result of the introduction of the thiophene ring, the overall performances of DSSCs prepared using CST and CDT dyes also improved. The most intense low-energy excitations of all the dyes examined in this work occurred from H → L transition.

3.5. Photovoltaic properties

The four sensitizers, CSI, CDI, CST and CDT, were incorporated into DSSCs with an I^-/I_3^- redox couple, and Fig. 8 shows the incident photon-to-current conversion efficiencies (IPCEs) of the corresponding DSSCs. The differences in photovoltaic performances of these DSSCs, as well as their power conversion efficiencies (PCEs), short-circuit photocurrent densities (J_{SC}), open-circuit photo-voltages (V_{OC}), and fill factors (FFs) were investigated under full sunlight and the results summarized in Table 4, and the J–V curves displayed in Fig. 9. Usually, an increase in the π-conjugation of the dyes broadens and shifts the spectral response towards the red region, which is crucial for enhanced light harvesting. As shown in Fig. 8, the devices lacking the thiophene spacer, CSI and CDI, showed higher values of IPCE of 10% and 14%, respectively, than CST and CDT. In the case of CST and CDT, the introduction of the thiophene spacer improved the width of their corresponding IPCE up to 800 nm. However, this introduction did not lead to an improvement in the magnitude of the IPCE values, producing lower photocurrent responses relative to those obtained with devices lacking the thiophene spacers (CSI and CDI).

As shown in Fig. 9, switching from single to double branched dyes produced an increase in both J_{SC} and V_{OC} values of the corresponding devices. In contrast, introducing the thiophene spacer between the donor and acceptor groups led to a prominent

decrease in J_{SC}. These outcomes are in good agreement with the calculated dye regeneration values discussed above. It is well known that the decrease in the LUMO energy of structurally similar dyes could decrease the Greg values to restore the ground state of the dye molecules. This could, in turn, result in severe reduction in IPCE values. In our results, the structurally similar single branched dyes CSI and CST exhibited a shifted bathochromically max. In particular, the IPCE dropped from 10% for the single branched dye absorbing at a max. of 487 nm to 8% for the single branched dye absorbing up to 770 nm (max. at 532 nm). A similar trend was observed for the double branched dyes. However, despite the decrease in the Greg values of the double branched dyes, overall, the current density and photo-voltage values were higher compared to those of single branched dyes owing to the fact that the double branched di-anchoring dyes could better insulate and attain higher adsorption on the NiO surface.

The power conversion efficiencies from highest to lowest were CDI > CDT > CSI > CST. It is clear that the DSSC devices with double branched di-anchoring dyes showed both higher J_{SC} and V_{OC} values, and in turn also PCEs compared to the singly branched dyes. Usually, the current-density values are positively correlated with the light-harvesting abilities of dye sensitizers. Nevertheless, contrary to previous reports, although the CDT exhibited the highest and broadest absorption spectrum, the value of J_{SC} of the p-DSSC based on CDT was lower than that achieved with CDI, and comparable with that of CSI. This result can be attributed to the lower dye regeneration driving force of CDT. Additionally, this result can be also explained by the fact that the CDT-based DSSC exhibited lower IPCE than those prepared with CSI and CDI, despite the broader nature of its IPCE. However, the presence of diethyl and dioctyl chains is highlighted in terms of the changes in V_{OC} values. This may be caused by the double branching, which could act as a better insulator. Subsequently, the increased number of alkyl chains as a result of the double branching could facilitate better use of inhibiting molecular aggregation on the photocathode film, which
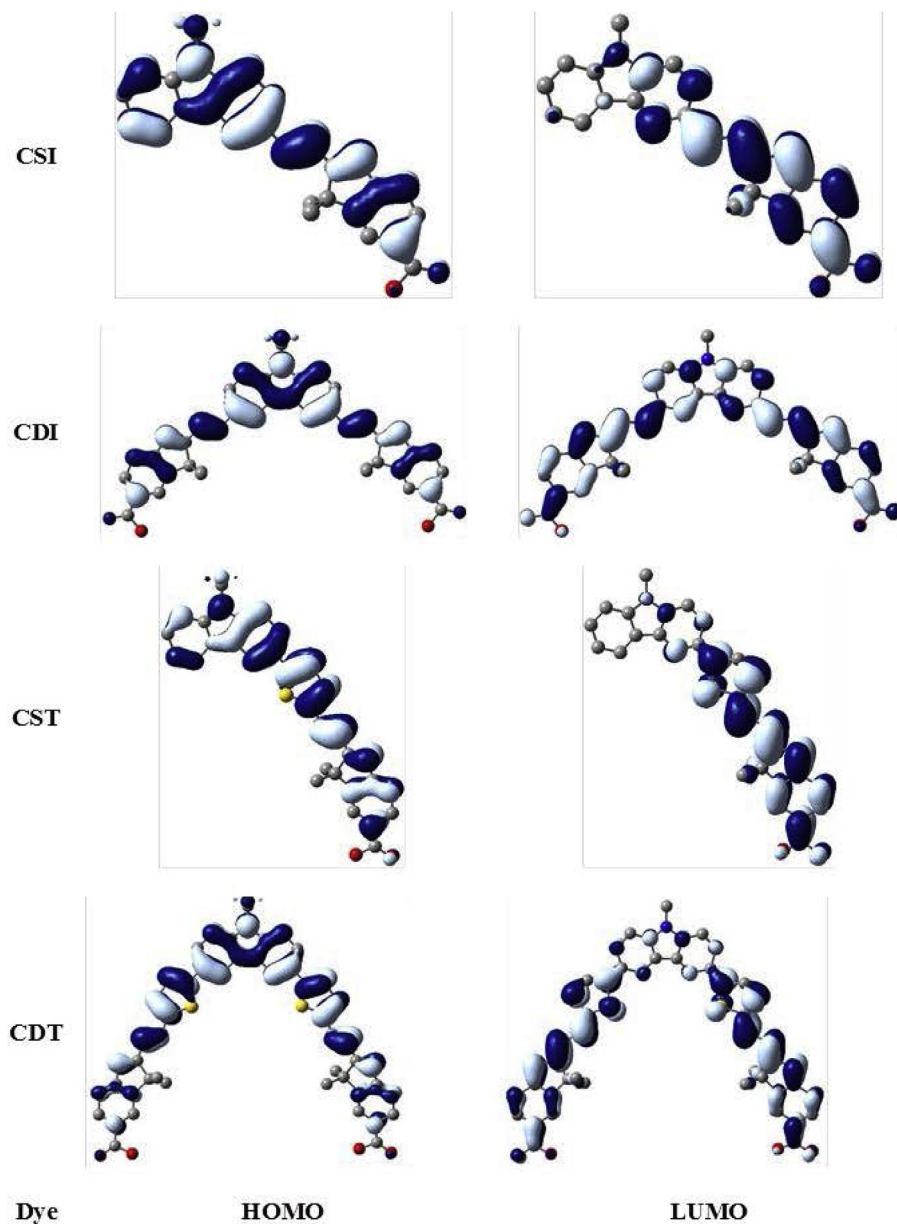
Fig. 6. Isodensity plots of frontier molecular orbitals of dyes CSI, CDI, CST, and CDT. Isosurface = 0.02 e $Å^{-3}$.

Table 2
Calculated Kohn-Sham eigenvalues of the frontier molecular orbitals and HLG values of CSI, CDI, CST, and CDT.

Dye	HOMO (eV)	LUMO (eV)	$\Delta_{\text{HOMO-LUMO}}$ (eV)
CSI	−5.88	−3.16	2.72
CDI	−6.13	−3.46	2.67
CST	−5.54	−3.34	2.20
CDT	−5.66	−3.46	2.20

decreases the possibility of hole recombination processes at the photoelectrode/dye/electrolyte interface, and enhances photovoltage.

3.6. Electrochemical impedance spectroscopy

We further employed electrochemical impedance analysis (EIS) to investigate the working principles of the prepared p-DSSCs. This analysis is a helpful tool for the interpretation of charge transport processes in electrochemical devices such as n-DSSCs and p-DSSCs [37,45]. Fig. 10 shows the results obtained for DSSCs comprised of FTO/NiO/dye electrodes. The major semicircles (R_{CT}) observed in the Nyquist plots (Fig. 10a) of all sensitizers were related to the resistance at the NiO/Dye/electrolyte interface. In our case, R_S and R_{CE} represent the FTO interface resistance and the resistance at the interface between the counter electrode/electrolyte, respectively. Owing to the fact that we employed the same Pt-coated counter electrode and the same electrolyte, the R_{CE} values of all devices did not show any significant variation. Similarly, the values of R_S of all sensitizers, which correspond to the intercept of the first semicircle in each case, showed similar results. In the present work, Warburg diffusion was not apparent and thus taken to be insignificant, most likely as a result of the fact that we employed a thin spacer (60 μm) and a low-viscosity solvent (acetonitrile). The results of fitting are listed in Table 5.

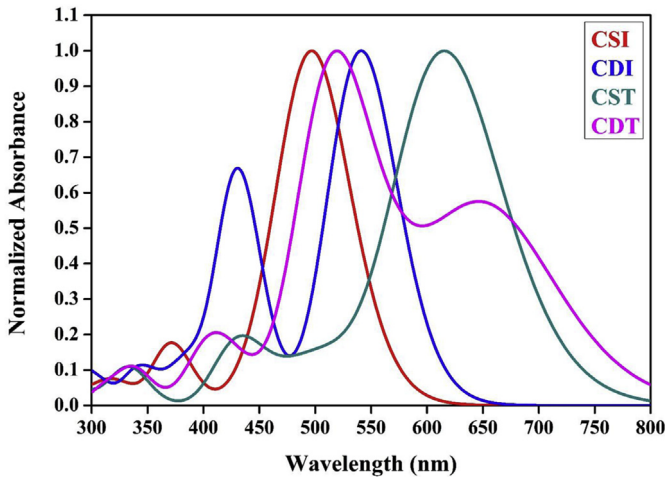Overall, the analysis showed that the R_{CT} values changed in

Fig. 7. Simulated UV-vis absorption spectra of CSI, CDI, CST, and CDT obtained at the TD-B3LYP/6-31G(d) level of theory. The spectra have been broadened using the Gaussian convolution with full-width half maximum (fwhm) = 3000 cm^{-1}.

Table 3
Calculated excitation wavelengths (λ_{cal}), oscillator strengths (f), and coefficients of configuration interaction (CI) with dominant contribution to each transition for CSI, CDI, CST, and CDT.

Dye	Transition	λ_{cal} (nm)	f	CI Coefficient	Dominant Contribution (%)
CSI	$S_0 \rightarrow S_1$	499	1.3393	0.6956	H → L (97)
	$S_0 \rightarrow S_2$	456	0.1754	0.6925	H-1 → L (96)
	$S_0 \rightarrow S_3$	371	0.2469	0.6919	H-2 → L (96)
	$S_0 \rightarrow S_4$	329	0.0614	0.6599	H-3 → L (87)
	$S_0 \rightarrow S_5$	313	0.0443	0.5856	H-4 → L (69)
CDI	$S_0 \rightarrow S_1$	541	1.7388	0.7027	H → L (99)
	$S_0 \rightarrow S_2$	468	0.0046	0.5008	H-1 → L (50)
	$S_0 \rightarrow S_3$	433	0.7275	0.5006	H → L+1 (50)
	$S_0 \rightarrow S_4$	427	0.4393	0.6932	H-1 → L+1 (96)
	$S_0 \rightarrow S_5$	385	0.2163	0.6743	H-2 → L (91)
CST	$S_0 \rightarrow S_1$	615	1.5690	0.7046	H → L (99)
	$S_0 \rightarrow S_2$	505	0.2183	0.6942	H-1 → L (96)
	$S_0 \rightarrow S_3$	433	0.3015	0.6885	H-2 → L (95)
	$S_0 \rightarrow S_4$	362	0.0070	0.6608	H-3 → L (87)
	$S_0 \rightarrow S_5$	342	0.0372	0.6766	H-4 → L (92)
CDT	$S_0 \rightarrow S_1$	660	1.0635	0.7031	H → L (99)
	$S_0 \rightarrow S_2$	593	0.3422	0.6688	H → L+1 (89)
	$S_0 \rightarrow S_3$	525	0.4414	0.6968	H-1 → L+1 (97)
	$S_0 \rightarrow S_4$	377	1.6695	0.6664	H-1 → L (89)
	$S_0 \rightarrow S_5$	430	0.1414	0.6933	H-2 → L (96)

Fig. 8. IPCE spectra of p-type DSSCs prepared with CSI, CDI, CST, and CDT as sensitizers.

Table 4
Photovoltaic performance of p-type DSSCs prepared with CSI, CDI, CST, and CDT, as sensitizers, with C343 as the reference (active area: 0.24 cm^2).

Dye	J_{SC} (mA/cm^2)	V_{OC} (V)	FF (%)	η (%)
C343	1.80	0.101	34.29	0.062
CSI	2.15	0.117	34.1	0.086
CDI	2.92	0.119	32.29	0.112
CST	2.09	0.109	32.11	0.073
CDT	2.15	0.135	32.67	0.095

Fig. 9. J–V characteristic spectra of p-type DSSCs prepared with CSI, CDI, CST, and CDT as sensitizers, with C343 as a reference.

accordance with the applied sensitizers, and the R_{CT} values for devices employing double branched dyes (44.70 Ω for CDI and 48.90 Ω for CDT) were indeed smaller than those of single branched dyes (66.75 Ω for CSI and 63.67 Ω for CST) owing to their increased charge transfer ability. Consequently, such decrease in the values of R_{CT} could result in improved photovoltaic performances. Fig. 10b shows the Bode phase plots of the corresponding devices. The frequency of the characteristic peak in the Bode phase plot increased in the order of CDT < CDI ≤ CSI < CST. A lower characteristic frequency in the Bode phase plot signifies a slower rate of charge recombination and higher V_{OC}. The reciprocal of the characteristic frequency is related to the hole lifetime and therefore, the electron lifetime increased in the order of CST < CSI ≤ CDI < CDT. This sequence of hole lifetimes obtained from the Bode phase plots showed increasing resistance to recombination. The lower R_{CT} values and longer electron lifetimes observed for double branched dyes (CDT/CDI) compared to the single branched dyes (CST/CSI) indicates more effective suppression of charge recombination. In
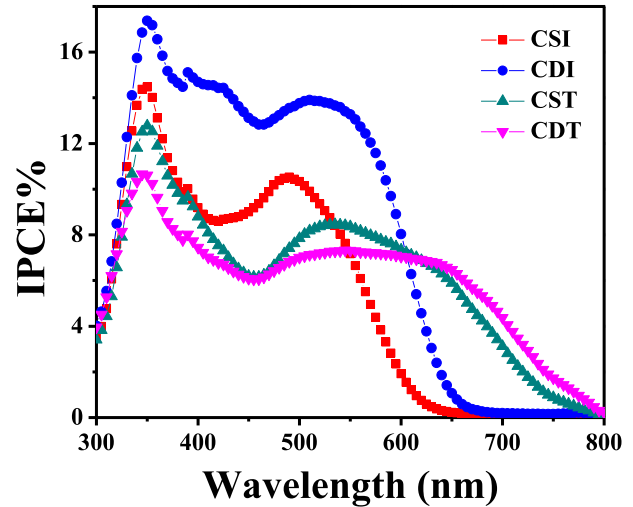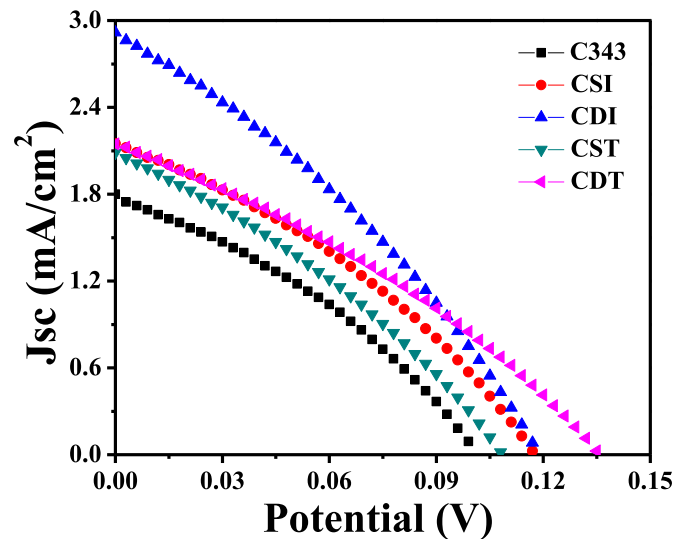
turn, this suppression is reflected in the improved J_{SC} and V_{OC} values, thus yielding a substantially enhanced power conversion efficiency.

By changing from single branched to double branched dyes, we noticed an enhancement in the values of V_{OC} for double branched dyes (CDI and CDT) relative to those of the single branched dyes (CSI and CST), which might arise as a result of their better surface coverage of NiO films. The obtained V_{OC} and electron lifetime values suggest that double branching with increased number of alkyl
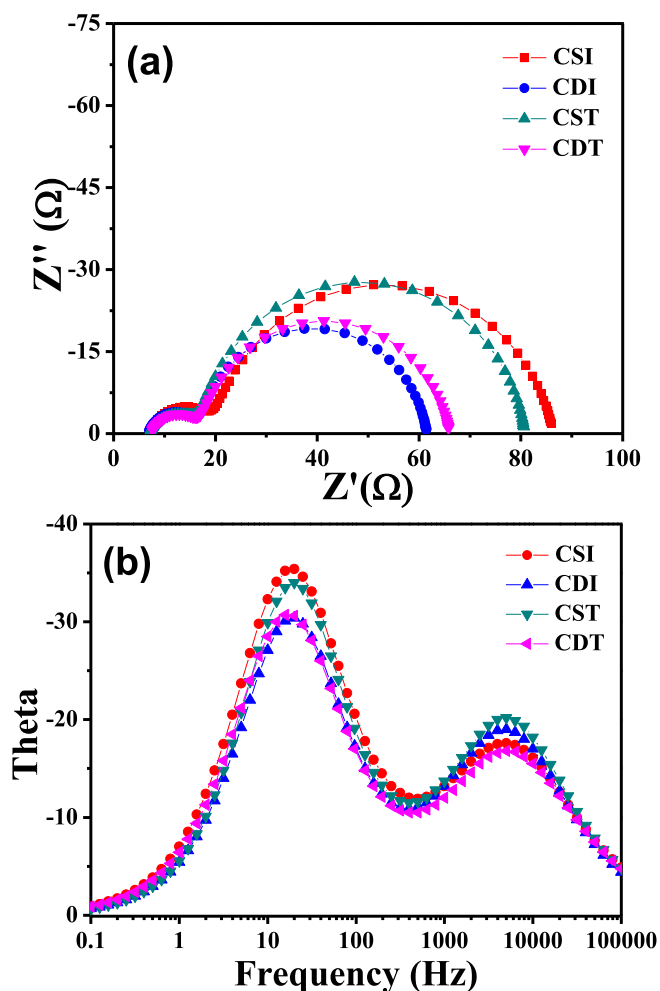
Fig. 10. Electrochemical impedance analysis of DSSCs prepared with CSI, CDI, CST, and CDT as sensitizers.

Table 5
Impedance analyses of DSSCs prepared with CSI, CDI, CST, and CDT as sensitizers.

Dye	$R_S^a(\Omega)$	$R_{CE}^b(\Omega)$	$R_{CT}^c(\Omega)$
CSI	7.277	12.39	66.75
CDI	6.83	10.00	44.70
CST	7.05	10.13	63.67
CDT	7.32	9.79	48.90

[a] R_S is FTO interface resistance.
[b] R_{CE} is due to the resistance at the interface between the counter electrode and the electrolyte.
[c] R_{CT} is the interfacial charge transfer resistance at the NiO/dye/electrolyte interface.

chains in CDI and CDT hampers the contact between the electrolyte and the charges generated in the devices. Therefore, the charge recombination rate on the NiO film decreases considerably, which in turn increases the electron lifetime on the NiO film, thus corroborating the higher V_{OC} values for CDI and CDT compared to CSI and CST.

4. Conclusions

In summary, we have synthesized four novel carbazole-based single and double branched cationic p-type dyes (CSI, CDI, CST, and CDT) and studied how branching and the presence of a thiophene spacer affect the photophysical and electrochemical properties in DSSC devices employing these dyes. These red-absorbing cationic p-type dyes compare favorably with the state-of-the-art dyes in terms of performance, which indicates that they could be utilized to enhance the photovoltaic performance of tandem devices in the future. We observed that both the introduction of a thiophene spacer, as well as switching from single to double branched dyes, caused the absorption maximum to shift to the red region of the visible spectrum. Consequently, the current density values increased from 2.15/2.09 mA/cm^2 (CSI/CST) to 2.92/2.15 mA/cm^2 (CDI/CDT). The EIS analysis showed that this difference stems to an extent from the differences in the interfacial charge transfer resistance values of these dyes, which were determined as 66.75/63.67 Ω and 44.70/48.90 Ω for single (CSI/CST) and double (CDI/CDT) branched dyes, respectively. We also found that branching or introduction of the thiophene spacer (in structurally similar dyes) lowered the LUMO levels and diminished the driving forces for dye regeneration. In addition, the photo-voltage values increased from 0.117/0.109 V (CSI/CST) to 0.119/0.135 V (CDI/CDT). Overall, increased branching led to increased J$_{SC}$ and V$_{OC}$ values, and ultimately produced increased power conversion efficiencies. This outcome can be most likely attributed to the effectiveness of interfacial charge transfer processes and the increased electron lifetime values of double anchored dyes. The electronic structures and both electrochemical and optical properties of the synthesized dyes were systematically studied through DFT/TDDFT simulations and the obtained results corroborated the experimental data. This study showed that the LUMO energy level of the dye sensitizer plays a key role in determining the photovoltaic performance of a p-DSSC.

Appendix A. Supplementary data

Supplementary data related to this article can be found at https://doi.org/10.1016/j.dyepig.2017.09.042.

References

[1] O'Regan B, Grätzel M. A low-cost, high-efficiency solar cell based on dye-sensitized colloidal TiO$_2$ films. Nature 1991;353:737–40.
[2] Hagfeldt A, Boschloo G, Sun L, Kloo L, Pettersson H. Dye-sensitized solar cells. Chem Rev 2010;110:6595–663.
[3] Clifford JN, Martinez-Ferrero E, Viterisi A, Palomares E. Sensitizer molecular structure-device efficiency relationship in dye sensitized solar cells. Chem Soc Rev 2011;40:1635–46.
[4] O'Regan BC, Durrant JR. Kinetic and energetic paradigms for dye-sensitized solar cells: moving from the ideal to the real. Acc Chem Res 2009;42:1799–808.
[5] Odobel F, Le Pleux L, Pellegrin Y, Blart E. New photovoltaic devices based on the sensitization of p-type semiconductors: challenges and opportunities. Acc Chem Res 2010;43:1063–71.
[6] Kakiage K, Aoyama Y, Yano T, Oya K, Fujisawa J, Hanaya M. Highly-efficient dye-sensitized solar cells with collaborative sensitization by silyl-anchor and carboxy-anchor dyes. Chem Commun 2015;51:15894–7.
[7] Mathew S, Yella A, Gao P, Humphry-Baker R, Curchod BFE, Ashari-Astani N, et al. Dye-sensitized solar cells with 13% efficiency achieved through the molecular engineering of porphyrin sensitizers. Nat Chem 2014;6:242–7.
[8] Zhang M, Wang Y, Xu M, Ma W, Li R, Wang P. Design of high-efficiency organic dyes for titania solar cells based on the chromophoric core of cyclopentadithiophene-benzothiadiazole. Energ Environ Sci 2013;6:2944–9.

[9] Chandrasekharam M, Suresh T, Singh SP, Priyanka B, Bhanuprakash K, Islam A, et al. Functionalized styryl bipyridine as a superior chelate for a ruthenium sensitizer in dye sensitized solar cells. Dalton Trans 2012;41:8770—2.

[10] Cuesta V, Vartanian M, Cruz de la P, Singhal R, Sharma GD, Langa F. Comparative study on the photovoltaic characteristics of A—D—A and D—A—D molecules based on Zn-porphyrin; a D—A—D molecule with over 8.0% efficiency. J Mater Chem A 2017;5:1057—65.

[11] Odobel F, Pellegrin Y, Gibson EA, Hagfeldt A, Smeigh AL, Hammarström L. Recent advances and future directions to optimize the performances of p-type dye-sensitized solar cells. Coord Chem Rev 2012;256:2414—23.

[12] Ren Y, Li Y, Chen S, Liu J, Zhanga J, Wang P. Improving the performance of dye-sensitized solar cells with electron-donor and electron-acceptor characteristic of planar electronic skeletons. Energy Environ Sci 2016;9:1390—9.

[13] Nattestad A, Mozer AJ, Fischer MKR, Cheng YB, Mishra A, Bäuerle P, et al. Highly efficient photocathodes for dye-sensitized tandem solar cells. Nat Mater 2010;9:31—5.

[14] Le Pleux L, Smeigh AL, Gibson E, Pellegrin Y, Blart E, Boschloo G, et al. Synthesis, photophysical and photovoltaic investigations of acceptor-functionalized perylene monoimide dyes for nickel oxide p-type dye-sensitized solar cells. Energ Environ Sci 2011;4:2075—84.

[15] Bonomo M, Sabuzi F, Carlo AD, Conte V, Dini D, Galloni P. KuQuinones as sensitizers for NiO based p-type dye-sensitized solar cells. New J Chem 2017;41:2769—79.

[16] Liu Z, Xiong D, Xu X, Arooj Q, Wang H, Yin L, et al. Modulated charge injection in p-type dye-sensitized solar cells using fluorene-based light absorbers. ACS Appl Mater Interfaces 2014;6:3448—54.

[17] Gibson EA, Smeigh AL, Le Pleux L, Fortage J, Boschloo G, Blart E, et al. A p-type NiO-based dye-sensitized solar cell with an open-circuit voltage of 0.35 V. Angew Chem Int Ed 2009;48:4402—5.

[18] Zhu H, Wu Y, Liu J, Zhang W, Wu W, Zhu WH. D—A—π—A featured sensitizers containing an auxiliary acceptor of benzoxadiazole: molecular engineering and co-sensitization. J Mater Chem A 2015;3:10603—9.

[19] Maufroy A, Favereau L, Anne FB, Pellegrin Y, Blart E, Hissler M, et al. Synthesis and properties of push-pull porphyrins as sensitizers for NiO based dye-sensitized solar cells. J Mater Chem A 2015;3:3908—17.

[20] Bonomo M, Barbero N, Matteocci F, Carlo AD, Barolo C, Dini D. Beneficial effect of electron-withdrawing groups on the sensitizing action of squaraines for p-type dye-sensitized solar cells. J Phys Chem C 2016;120:16340—53.

[21] Lefebvre JF, Sun XZ, Calladine JA, George MW, Gibson A. Promoting charge-separation in p-type dye-sensitized solar cells using bodipy. Chem Commun 2014;50:5258—60.

[22] Kong W, Li S, Chen Z, Wei C, Li W, Li T, et al. p-Type dye-sensitized solar cells with a CdSeS quantum-dot-sensitized NiO photocathode for outstanding short-circuit current. Part Part Syst Charact 2015;32:1078—82.

[23] Park JY, Suresh T, Yun HJ, Lee CH, Ahn KS, Kim JH. Synthesis and investigation of the donor effect in novel hemicyanine organic dyes for p-type dye-sensitized solar cells. Sci Adv Mater 2016;8:589—95.

[24] He J, Lindström H, Hagfeldt A, Lindquist SE. Dye-sensitized nanostructured tandem cell-first demonstrated cell with a dye-sensitized photocathode. Sol Energy Mater Sol Cells 2000;62:265—73.

[25] Shao Z, Pan X, Chen H, Tao L, Wang W, Ding Y, et al. Polymer based photocathodes for panchromatic tandem dye-sensitized solar cells. Energy Environ Sci 2014;7:2647—51.

[26] Powar S, Bhargava R, Daeneke T, Götz G, Bäuerle P, Geiger T, et al. Thiolate/disulfide based electrolytes for p-type and tandem dye-sensitized solar cells. Electrochim Acta 2015;182:458—63.

[27] Ho P, Thogiti S, Lee YH, Kim JH. Discrete photoelectrodes with dyes having different absorption wavelengths for efficient cobalt based tandem dye-sensitised solar cells. Sci Rep 2017;7:2272.

[28] Wood CJ, Summers GH, Gibson EA. Increased photocurrent in a tandem dye-sensitized solar cell by modifications in push-pull dye-design. Chem Commun 2015;51:3915—8.

[29] Ooyama Y, Harima Y. Photophysical and electrochemical properties, and molecular structures of organic dyes for dye-sensitized solar cells. ChemPhysChem 2012;13:4032—80.

[30] El-Shafei A, Hussain M, Atiq A, Islam A, Han L. Novel carbazole-based dye outperformed the benchmark dye N719 for high efficiency dye-sensitized solar cells (DSSCs). J Mater Chem 2012;22:24048—56.

[31] Koumura N, Wang ZS, Miyashita M, Uemura Y, Sekiguchi H, Cui Y, et al.

Substituted carbazole dyes for efficient molecular photovoltaics: long electron lifetime and high open circuit voltage performance. J Mater Chem 2009;19:4829—36.

[32] Soni SS, Fadadu KB, Vaghasiya JV, Solanki BG, Sonigara KK, Singh A, et al. Improved molecular architecture of D—π—A carbazole dyes: 9% PCE with a cobalt redox shuttle in dye sensitized solar cells. J Mater Chem A 2015;3:21664—71.

[33] Kakiage K, Aoyama Y, Yano T, Oya K, Kyomen T, Hanaya M. Fabrication of a high-performance dye-sensitized solar cell with 12.8% conversion efficiency using organic silyl-anchor dyes. Chem Commun 2015;51:6315—7.

[34] Venkateswararao A, Justin Thomas KR, Lee CP, Li CT, Ho KC. Organic dyes containing carbazole as donor and π-linker: optical, electrochemical, and photovoltaic properties. ACS Appl Mater Interfaces 2014;6:2528—39.

[35] Cho JM, Thogiti S, Cheruku R, Lee DK, Ahn KS, Kim JH. Influence of different electron acceptors in carbazole-based organic sensitizers on the performance of dye-sensitized solar cells. J Nanosci Nanotechnol 2017;17:3316—22.

[36] Wood CJ, Cheng M, Clark CA, Horvath R, Clark IP, Hamilton ML, et al. Red-absorbing cationic acceptor dyes for photocathodes in tandem solar cells. J Phys Chem C 2014;118:16536—46.

[37] Park JY, Jang BY, Lee CH, Yun HJ, Kim JH. Influence of the anchoring number in a carbazole-based photosensitizer on the photovoltaic performance of p-type NiO dye sensitized solar cells. RSC Adv 2014;4:61248—55.

[38] Bao LQ, Hai NT, Thogiti S, Kim JH. Synthesis and investigation of number of anchoring and spacer effect in triphenylamine-based organic dyes for p-type dye sensitized solar cells. Sci Adv Mater 2017;9:161—7.

[39] Chang CH, Chen YC, Hsu CY, Chou HH, Lin JT. Squaraine-arylamine sensitizers for highly efficient p-type dye-sensitized solar cells. Org Lett 2012;14:4726—9.

[40] Cao D, Jinan P, Yanping H, Xiaoming F, Herbert M. Enhanced performance of the dye-sensitized solar cells with phenothiazine-based dyes containing double D—A branches. Org Lett 2011;13:1610—3.

[41] Chen YC, Lin JT. Multi-anchored sensitizers for dye-sensitized solar cells. Sustain Energy Fuels 2017;1:969—85.

[42] Zu-Sheng H, Cheng C, Xu-Feng Z, Zafar I, Derong C. Effect of the linkage location in double branched organic dyes on the photovoltaic performance of DSSCs. J Mater Chem A 2015;3:1333—44.

[43] Ren X, Jiang S, Cha M, Zhou G, Wang ZS. Thiophene-bridged double d-π-a dye for efficient dye-sensitized solar cell. Chem Mater 2012;24:3493—9.

[44] Park JH, Jang BY, Thogiti S, Ryu JH, Kim SH, Son YA, et al. A comparison of the optical and photovoltaic properties of novel double branched organic dyes in dye sensitized solar cells. Synth Met 2015;203:235—42.

[45] Lee YH, Chitumalla RK, JangBY Jang J, Thogiti S, Kim JH. Alkyl chain length dependence of the charge-transfer, recombination and electron diffusion length on the photovoltaic performance in double donor-acceptor-based organic dyes for dye sensitized solar cells. Dyes Pigm 2016;133:161—72.

[46] Frisch MJ, Trucks GW, Schlegel HB, Scuseria GE, Cioslowski J, Fox DJ, et al. Wallingford CT. 2009.

[47] Becke AD. Density-functional thermochemistry. III. The role of exact exchange. J Chem Phys 1993;98:5648—52.

[48] Becke AD. Density-functional thermochemistry. IV. A new dynamic correlation functional and implications for exact-exchange mixing. J Chem Phys 1996;104:1040—6.

[49] Lee C, Yang W, Parr RG. Development of the Colle-Salvetti correlation-energy formula into a functional of the electron density. Phys Rev B 1988;37:785—9.

[50] Miertuš S, Scrocco E, Tomasi J. Electrostatic interaction of a solute with a continuum. A direct utilization of ab initio molecular potentials for the prevision of solvent effects. Chem Phys 1981;55:117—29.

[51] Cossi M, Barone V, Cammi R, Tomasi J. Ab initio study of solvated molecules: a new implementation of the polarizable continuum model. Chem Phys Lett 1996;255:327—35.

[52] Preat J, Hagfeldt A, Perpète EA. Investigation of the photoinduced electron injection processes for p-type triphenylamine-sensitized solar cells. Energy Environ Sci 2011;4:4537—49.

[53] Zhang T, Guan W, Yan L, Ma T, Wang J, Su Z. Theoretical studies on POM-based organic—inorganic hybrids containing double D—A1—π—A2 chains for high-performance p-type, dye-sensitized solar cells (DSSCs). Phys Chem Chem Phys 2015;17:5459—65.

[54] Grimme S, Parac M. Substantial errors from time-dependent density functional theory for the calculation of excited states of large π systems. ChemPhysChem 2003;4:292—5.